

# Small-Signal Modeling and Control of ZVT-PWM Boost Converters

Jong-Lick Lin, *Member, IEEE*, and Chin-Hua Chang

**Abstract**—A small-signal model for zero-voltage-transition pulse width modulation (ZVT-PWM) boost converters is derived in this paper. The accuracy of the developed model is verified by experimental measurement. It shows that the ZVT-PWM boost converters exhibit better dynamical behavior than the conventional PWM boost converters. To achieve output voltage regulation and line voltage disturbance rejection of ZVT-PWM boost converters, a classical controller and a modified integral variable structure controller are designed. The output voltage regulation in the presence of line voltage and load variations for both controllers are compared by experimental results.

**Index Terms**—Modified integral variable structure control, small-signal model, ZVT-PWM soft-switching boost converter.

## I. INTRODUCTION

THE ZVT-PWM soft-switching converters [1]–[3] solve the existing problems of high switching losses of conventional PWM converters and high voltage and current stresses of resonant converters. By taking advantages of pulse width modulation and tank resonance, the soft-switching boost power converters with constant frequency operation are considered in this paper. These kinds of converters are especially useful in the application of high efficiency power converter systems.

In the literature, all research on ZVT-PWM soft-switching converters have been restricted to steady-state analysis. The assumption that the small-signal model should be the same as conventional PWM DC-DC converters is not confirmative. Therefore, a small-signal model for a ZVT-PWM boost converter is developed in this paper. The differences between ZVT-PWM and conventional PWM boost converters are shown by comparing their dynamical models. The main purpose to derive a mathematical model is required for controller design to achieve output voltage regulation and line voltage disturbance rejection.

In this paper, the averaging method for two-time-scale discontinuous system (AM-TTS-DS) [4] is used to derive a small-signal model of ZVT-PWM boost converters. The model is verified by experimental results. Then based on this model, a classical controller and a modified integral variable structure controller (MIVSC) [5] are designed. Finally, the overall system is implemented in the laboratory and the system performances for the two controllers are compared.

Manuscript received September 3, 1999; revised October 1, 2002. This work was supported by the National Science Council of the Republic of China, under Grant Contract NSC 88-2213-E-006-095. Recommended by Associate Editor M. A. Rahman.

The authors are with the Department of Engineering Science, National Cheng Kung University, Tainan, Taiwan 701, ROC (e-mail: jllin@mail.ncku.edu.tw).  
Digital Object Identifier 10.1109/TPEL.2002.807176

## II. ZVT-PWM BOOST CONVERTERS

A ZVT-PWM soft-switching boost converter [3] is shown in Fig. 1. It includes a conventional PWM boost converter drawn with thin lines and some additional components drawn with thick lines. The additional components are composed of a resonant tank, auxiliary diode  $D_2$  and snubber capacitor  $C_s$ . The resonant tank includes an auxiliary switch  $S_2$  and resonant inductor  $L_r$  and capacitor  $C_r$ .

The zero-voltage soft switching of the main switch  $S_1$  is achieved by tank resonance which is controlled by the auxiliary switch  $S_2$ . From a circuit point of view, the system operation in one switching period  $T_s$  can be divided into eight linear circuit stages. The key waveforms at steady state are shown in Fig. 2. All switching components work in soft-switching conditions without extra voltage/current peaks except  $S_1$  suffering from larger current spike in stage 4 of time interval  $[t_3, t_4]$ .

The detailed analysis of circuit operations was proposed in [3]. The steady-state analysis for stages 1 and 2 are shown as follows.

*Stage 1* (see Fig. 3): The auxiliary switch  $S_2$  turns on at  $t_0$ . Current starts to flow through the resonant tank and the resonance occurs. Circuit analysis gives

$$i_{Lr}(t) = \frac{V_o}{Z_1} \sin \omega_1(t - t_0) \quad (1)$$

$$v_{C_s}(t) = V_o \quad (2)$$

$$v_{C_r}(t) = V_o - V_o \cos \omega_1(t - t_0) \quad (3)$$

for  $t_0 \leq t \leq t_1$  with  $Z_1 \triangleq \sqrt{L_r/C_r}$  and  $\omega_1 = 1/\sqrt{L_r C_r}$ .

*Stage 2* (see Fig. 4): When  $i_{Lr}$  becomes greater than  $I_{Lm}$ ,  $D_1$  turns off and stage 2 starts. The increasing current  $i_{Lr} - I_{Lm}$  offered by  $C_s$  leads to the decreasing of  $v_{C_s}$ . Circuit analysis yields

$$i_{Lr}(t) = \frac{V_1}{Z_2} \sin \omega_2(t - t_1) + I_1 \cos \omega_2(t - t_1) + \frac{C_r}{C_r + C_s} I_{Lm} \quad (4)$$

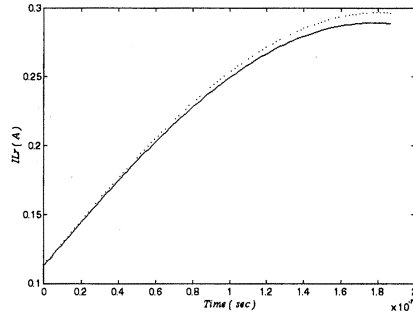
$$v_{C_s}(t) = \frac{C}{C_s} [V_1 \cos \omega_2(t - t_1) - I_1 Z_2 \sin \omega_2(t - t_1) - V_1] + \frac{I_{Lm}}{C_r + C_s} (t - t_1) + V_o \quad (5)$$

$$v_{C_r}(t) = \frac{C}{C_r} [-V_1 \cos \omega_2(t - t_1) + I_1 Z_2 \sin \omega_2(t - t_1) + V_1] + \frac{I_{Lm}}{C_r + C_s} (t - t_1) + v_{C_r}(t_1) \quad (6)$$

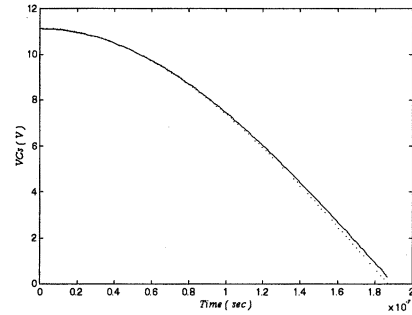


TABLE I  
VOLTAGES AND CURRENTS AT EACH STAGE

	$v_{Cs}(t)$	$v_{Cr}(t)$	$i_{Lr}(t)$	$i_{D1}(t)$	$i_{D2}(t)$	$T_i, i=1,2,\dots,8$
$[t_0, t_1]$	$V_o$	0	$\frac{V_o}{L_r}(t-t_0)$	$I_{Lm}-i_{Lr}(t)$	0	$\frac{L_r I_{Lm}}{V_o}$
$[t_1, t_2]$	$\frac{C}{C_s} V_o \cos \omega_2(t-t_1) + \frac{C}{C_s} V_o$	equation (6)	$\frac{V_o}{Z_2} \sin \omega_2(t-t_1) + I_{Lm}$	0	0	$\frac{1}{\omega_2} \cos^{-1} \left( -\frac{C_s}{C_r} \right)$
$[t_2, t_3]$	0	$v_{Cr}(t_2) \cos \omega_1(t-t_2) + i_{Lr}(t_2) Z_1 \sin \omega_1(t-t_2)$	$i_{Lr}(t_2) \cos \omega_1(t-t_2) - \frac{v_{Cr}(t_2)}{Z_1} \sin \omega_1(t-t_2)$	0	0	$\frac{1}{\omega_1} \left( \frac{\pi}{2} - \sin^{-1} \left( \frac{v_{Cr}(t_2)}{v_{Cr,p}} \right) \right)$
$[t_3, t_4]$	0	$v_{Cr,p} \cos \omega_1(t-t_3)$	$-\frac{v_{Cr,p}}{Z_1} \sin \omega_1(t-t_3)$	0	0	$\frac{\pi}{\omega_1}$
$[t_4, t_5]$	0	$-v_{Cr,p}$	0	0	0	$dT_2 - (T_1 + T_2 + T_3 + T_4)$
$[t_5, t_6]$	$\frac{I_{Lm}}{C_s}(t-t_5)$	$-v_{Cr,p}$	0	0	0	$(V_o - v_{Cr,p}) \frac{C_s}{I_{Lm}}$
$[t_6, t_7]$	$v_r - v_{o,r} + \frac{I_{Lm}}{C_s + C_r}(t-t_6)$	$-v_{o,r} + \frac{I_{Lm}}{C_s + C_r}(t-t_6)$	0	0	$\frac{C_r}{C_s + C_r} I_{Lm}$	$(C_s + C_r) \frac{v_{Cr,p}}{I_{Lm}}$
$[t_7, (t_7 + T_7)]$	$V_o$	0	0	$I_{Lm}$	0	$dT_5 - (T_6 + T_7)$



(a)



(b)

Fig. 5. Exact and approximate solutions: (a)  $i_{Lr}(t)$  and (b)  $v_{Cs}(t)$ .

by boundary condition  $v_{Cs}(t_2) = 0$ . Substituting (13) into (10) yields

$$\begin{aligned} i_{Lr}(t_2) &\approx \frac{V_o}{Z_2} \sin \omega_2 T_2 + I_{Lm} \\ &= \frac{V_o}{Z_2} \frac{\sqrt{C_r^2 - C_s^2}}{C_r} + I_{Lm}. \end{aligned} \quad (14)$$

The approximation results with load  $R_L = 200 \Omega$  are shown in Fig 5. The exact solutions for  $i_{Lr}(t)$  in (4) and  $v_{Cs}(t)$  in (5) are shown with solid lines, and the corresponding approximate solutions in (10) and (11) are shown with dotted lines. It is seen that the approximation results are very close to the exact solutions, and thus the simplification is reasonable.

#### IV. CALCULATIONS OF $v_{Cr}(t_3)$ AND $v_{Cr}(t_2)$ IN TABLE I

For the convenience in latter analysis, the capacitor voltages  $v_{Cr}(t_2)$  and  $v_{Cr,p} \triangleq v_{Cr}(t_3)$  in Table I are now calculated. Since

elements  $C_s$ ,  $C_r$  and  $L_r$  are all power lossless, from an energy conservation point of view we conclude that

$$\begin{aligned} &\text{total energy stored in } C_s, C_r \text{ and } L_r \text{ at } t_3 \\ &= \text{total energy stored in } C_s, C_r \text{ and } L_r \text{ at } t_2 \\ &= \text{total energy stored in } C_s, C_r \text{ and } L_r \text{ at } t_1 \text{ plus} \\ &\text{energy supplied by } I_{Lm} \text{ from } t_1 \text{ to } t_2. \end{aligned} \quad (15)$$

It follows from the second equality in (15) and  $v_{Cs}(t_3) = 0$ ,  $i_{Lr}(t_3) = 0$  and,  $v_{Cr}(t_1) = 0$  that

$$\begin{aligned} \frac{1}{2} C_r v_{Cr}^2(t_3) &= \int_{t_1}^{t_2} I_{Lm} v_{Cs}(t) dt + \frac{1}{2} C_s v_{Cs}^2(t_1) + \frac{1}{2} L_r i_{Lr}^2(t_1) \\ &= k I_{Lm} V_o + \frac{1}{2} C_s V_o^2 + \frac{1}{2} L_r I_{Lm}^2 \end{aligned} \quad (16)$$

where

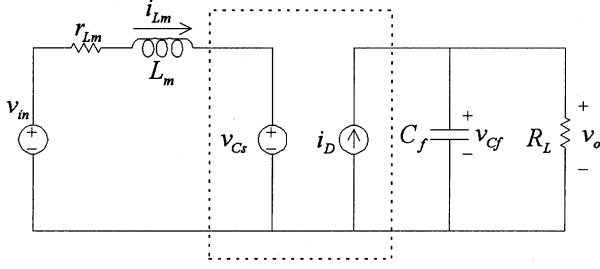


Fig. 6. Equivalent circuit model of the ZVT-PWM boost converter.

$$k \triangleq \frac{1}{\omega_2} \sqrt{\frac{C_r - C_s}{C_r + C_s}} + \frac{C}{C_r} \frac{1}{\omega_2} \cos^{-1} \left( -\frac{C_s}{C_r} \right) \approx \sqrt{C_s L_r} \quad (17)$$

and thus we have

$$v_{C_r}(t_3) = \sqrt{2 \frac{k}{C_r} I_{L_m} V_o + \frac{C_s}{C_r} V_o^2 + \frac{L_r}{C_r} I_{L_m}^2} \approx \sqrt{\frac{C_s}{C_r} V_o} + \sqrt{\frac{L_r}{C_r}} I_{L_m} \quad (18)$$

from (16). Moreover, following from the first equality in (15) and  $v_{C_s}(t_3) = 0$ ,  $i_{L_r}(t_3) = 0$  and  $v_{C_s}(t_2) = 0$  gives

$$\frac{1}{2} C_r v_{C_r}^2(t_3) = \frac{1}{2} L_r i_{L_r}^2(t_2) + \frac{1}{2} C_r v_{C_r}^2(t_2). \quad (19)$$

Together with (14) and (18), we get

$$v_{C_r}(t_2) = \sqrt{\frac{C_r v_{C_r}^2(t_3) - L_r i_{L_r}^2(t_2)}{C_r}}. \quad (20)$$

The resonant currents, voltages and duration of each stage are summarized in Table I.

## V. MATHEMATICAL MODEL DERIVATION

The small-signal model of the ZVT-PWM boost converter shown in Fig. 1 will be derived based on AM-TTS-DS [4]. The ZVT-PWM boost converter can be divided into two subcircuits, a fast subcircuit and a slow subcircuit. The former includes fast state variables  $v_{C_s}(t)$ ,  $v_{C_r}(t)$  and  $i_{L_r}(t)$ . The latter includes slow state variables  $i_{L_m}(t)$  and  $v_{C_f}(t)$ . The equivalent circuit model of the ZVT-PWM boost converter is shown in Fig. 6 where the part enclosed by dotted line is the equivalent fast subcircuit. Current  $i_D(t)$  is the sum of diode currents  $i_{D1}(t)$  and  $i_{D2}(t)$  in Fig. 1.

The ZVT-PWM boost converters are used to obtain a well regulated output voltage  $v_o(t)$  which is just the slow state variable of the capacitor voltage  $v_{C_f}(t)$ . From a fast subcircuit point of view, the slow state variables in Fig. 1 can be treated as constants. This leads to the results in Section II that  $i_{L_m} \approx I_{L_m}$  and  $v_{C_f} \approx V_{C_f} = V_o$ . On the contrary, from a slow subcircuit point of view, only averaging behaviors of the fast state variables have effects on the slow state variables. As a result, substituting the fast variables by their moving averages, the averaged model

of the slow subcircuit is then obtained. Viewing this, the state equation of the equivalent circuit model in Fig. 6 is given by

$$\begin{aligned} \frac{di_{L_m}(t)}{dt} &= \frac{v_{in}(t)}{L_m} - \frac{r_{L_m}}{L_m} i_{L_m}(t) - \frac{v_{C_s}(t)}{L_m} \\ \frac{dv_{C_f}(t)}{dt} &= -\frac{v_{C_f}(t)}{C_f R_L} + \frac{i_D(t)}{C_f} \end{aligned} \quad (21)$$

with output equation

$$v_o(t) = v_{C_f}(t). \quad (22)$$

Then, taking the moving average for  $v_{C_s}(t)$  and  $i_D(t)$  listed in Table I, the state-space averaged model of (21) can be expressed as

$$\begin{aligned} \frac{di_{L_m}(t)}{dt} &= \frac{v_{in}(t)}{L_m} - \frac{r_{L_m}}{L_m} i_{L_m}(t) - \frac{1}{L_m} v_{C_f}(t) [d'(t) + \delta_1(t)] \\ \frac{dv_{C_f}(t)}{dt} &= -\frac{v_{C_f}(t)}{C_f R_L} + \frac{1}{C_f} i_{L_m}(t) [d'(t) + \delta_2(t)] \end{aligned} \quad (23)$$

where  $d'(t)$ ,  $\delta_1(t)$  and  $\delta_2(t)$  are defined by

$$d'(t) \triangleq 1 - d(t) = \frac{T_6(t) + T_7(t) + T_8(t)}{T_s} \quad (24)$$

$$\delta_1(t) \triangleq \frac{a_1 v_{C_f}(t)}{T_s i_{L_m}(t)} + \frac{a_2}{T_s} + \frac{a_3 i_{L_m}(t)}{T_s v_{C_f}(t)} \quad (25)$$

$$\delta_2(t) \triangleq -\frac{C_s v_{C_f}(t)}{T_s i_{L_m}(t)} + \frac{L_r i_{L_m}(t)}{2 T_s v_{C_f}(t)} \quad (26)$$

with

$$a_1 \triangleq \frac{C_s^2}{C_r} - (C_r + C_s) \sqrt{\frac{C_s}{C_r}} \quad (27)$$

$$a_2 \triangleq (C_r + C_s) \left( \frac{2k}{C_r} - \sqrt{\frac{L_r}{C_r}} \right) \quad (28)$$

$$a_3 \triangleq \frac{(3C_r + 2C_s)L_r}{2C_r}. \quad (29)$$

With the help of the notation, (23) can also be rewritten as a nonlinear and time-invariant state equation

$$\begin{aligned} \begin{bmatrix} \dot{i}_{L_m}(t) \\ \dot{v}_{C_f}(t) \end{bmatrix} &= \begin{bmatrix} -\frac{r_{L_m}}{L_m} & -\frac{d'(t)}{L_m} \\ \frac{d'(t)}{C_f} & -\frac{1}{C_f R_L} \end{bmatrix} \begin{bmatrix} i_{L_m}(t) \\ v_{C_f}(t) \end{bmatrix} + \begin{bmatrix} \frac{1}{L_m} \\ 0 \end{bmatrix} v_{in}(t) \\ &+ \begin{bmatrix} \frac{\partial_1(t)}{L_m} v_{C_f}(t) \\ \frac{\partial_2(t)}{C_f} I_{L_m}(t) \end{bmatrix} \end{aligned} \quad (30)$$

and output equation

$$v_o(t) = [0 \ 1] \begin{bmatrix} i_{L_m}(t) \\ v_{C_f}(t) \end{bmatrix}. \quad (31)$$

It is interesting to note that (30) becomes the dynamical equation of the conventional PWM boost converters if both  $\delta_1(t)$  and  $\delta_2(t)$  inside the last bracket in (30) vanish.

To obtain the linearized state equation, the nonlinear equation (30) is expanded into the Taylor series around the nominal operating point Q, and then the higher order nonlinear terms

are neglected. The nominal operating point can be easily obtained by setting  $di_{Lm}/dt = 0$  and  $d\nu_{Cf}/dt = 0$  in (30). Introducing  $p_1 \triangleq (a_1)/(T_s)$ ,  $p_2 \triangleq (a_2)/(T_s) + D'$ ,  $p_3 \triangleq (a_3)/(T_s) + r_{Lm}$ ,  $p_4 \triangleq -V_{in}$ ,  $q_1 \triangleq -(1/(R_L) + (C_s)/(T_s))$ ,  $q_2 \triangleq D'$  and  $q_3 \triangleq (L_r)/(2T_s)$ , the mathematical manipulation gives

$$\begin{aligned} p_1 V_o^2 + p_2 V_o I_{Lm} + p_3 I_{Lm}^2 + p_4 I_{Lm} &= 0 \\ q_1 V_o^2 + q_2 V_o I_{Lm} + q_3 I_{Lm}^2 &= 0. \end{aligned} \quad (32)$$

The solutions for  $V_o$  and  $I_{Lm}$  in (32) are given by

$$\begin{aligned} V_o &= \frac{wq_3p_1 - wq_1p_3 - q_1p_4}{p_2q_1 - q_2p_1} p_4 \\ I_{Lm} &= wp_4 \end{aligned} \quad (33)$$

with  $w \triangleq (-b + \sqrt{b^2 - 4ac})/2a$ , where

$$a = q_3^2 p_1^2 - 2q_3 p_1 q_1 p_3 + q_1^2 p_3^2 - p_2 q_2 p_1 q_3 - p_2 q_2 q_1 p_3 + p_2^2 q_1 q_3 + p_3 q_2^2 p_1 \quad (34)$$

$$b = q_1^2 p_3 - 2q_3 p_1 q_1 + q_2^2 p_1 - p_2 q_2 q_1 \quad (35)$$

$$c = q_1^2. \quad (36)$$

With the help of (33), it leads to the conclusion that

$$\frac{V_o}{V_{in}} = \frac{I_{Lm}}{I_o} = \frac{I_{Lm}}{V_o/R_L} \approx \frac{1}{D'} \quad (37)$$

which approximates to the voltage gain of the conventional PWM boost converter. Then, by introducing small perturbations around the operating point

$$\begin{aligned} i_{Lm} &= I_{Lm} + \tilde{i}_{Lm}, \nu_{Cf} = V_{Cf} + \tilde{\nu}_{Cf}, \\ \nu_o &= V_o + \tilde{\nu}_o, d = D + \tilde{d} \\ d' &= 1 - d = 1 - (D + \tilde{d}) = D' - \tilde{d}, \\ \nu_{in} &= V_{in} + \tilde{\nu}_{in} \end{aligned} \quad (38)$$

with

$$\begin{aligned} |\tilde{i}_{Lm}| &\ll I_{Lm}, |\tilde{\nu}_{Cf}| \ll V_{Cf}, |\tilde{\nu}_o| \ll V_o, \\ |\tilde{d}| &\ll D, |\tilde{\nu}_{in}| \ll V_{in} \end{aligned} \quad (39)$$

it is verified that

$$\begin{aligned} \begin{bmatrix} \tilde{i}_{Lm} \\ \tilde{\nu}_{Cf} \end{bmatrix} &= \begin{bmatrix} -\frac{r_{Lm}}{L_m} + k_{1i_{Lm}} & -\frac{D'}{L_m} + k_{1\nu_{Cf}} \\ \frac{D'}{C_f} + k_{2i_{Lm}} & -\frac{1}{R_L C_f} + k_{2\nu_{Cf}} \end{bmatrix} \begin{bmatrix} \tilde{i}_{Lm} \\ \tilde{\nu}_{Cf} \end{bmatrix} \\ &+ \begin{bmatrix} \frac{1}{L_m} & \frac{V_o}{L_m} \\ 0 & -\frac{I_{Lm}}{C_f} \end{bmatrix} \begin{bmatrix} \tilde{\nu}_{in} \\ \tilde{d} \end{bmatrix} \\ \tilde{\nu}_o &= [0 \ 1] \begin{bmatrix} \tilde{i}_{Lm} \\ \tilde{\nu}_{Cf} \end{bmatrix} \end{aligned} \quad (40)$$

where

$$\begin{aligned} k_{1i_{Lm}} &\triangleq \left. \frac{\partial \delta_{o1}}{\partial i_{Lm}} \right|_Q = \frac{a_1}{L_m T_s} \left( \frac{V_o}{I_{Lm}} \right)^2 - \frac{a_3}{L_m T_s} \\ &\approx \frac{a_1}{L_m T_s} (R_L D')^2 - \frac{a_3}{L_m T_s} \end{aligned} \quad (41)$$

$$k_{1\nu_{Cf}} \triangleq \left. \frac{\partial \delta_{o1}}{\partial \nu_{Cf}} \right|_Q = -\frac{2a_1}{L_m T_s} \frac{V_o}{I_{Lm}} - \frac{a_2}{L_m T_s}$$

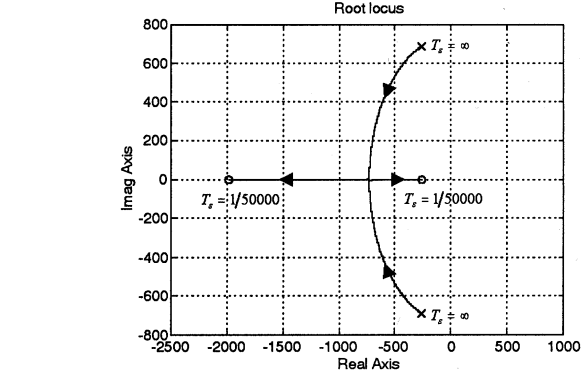


Fig. 7. Root locus for ZVT-PWM converter as a function of switching period  $T_s$ .

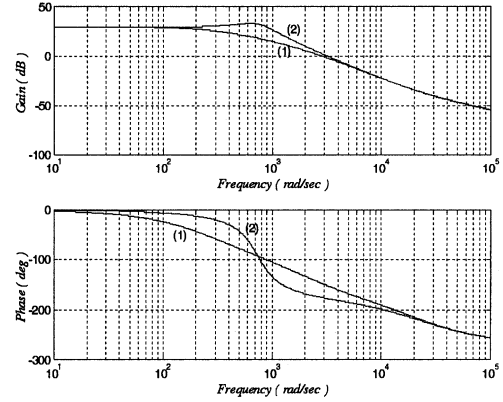


Fig. 8. Bode plot of  $\bar{\nu}_o(s)/\bar{d}(s)$ : (1) ZVT-PWM boost converter and (2) conventional boost converter.

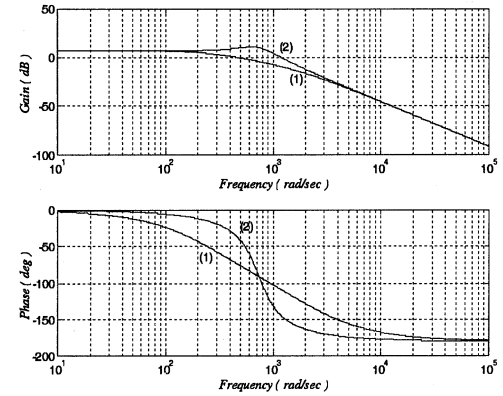


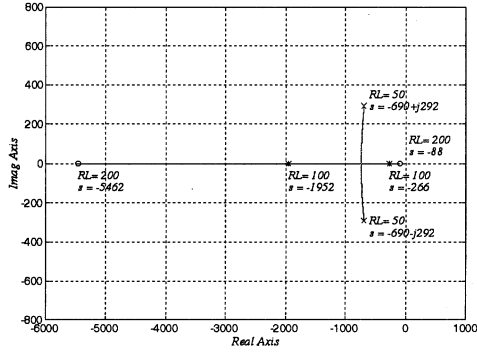
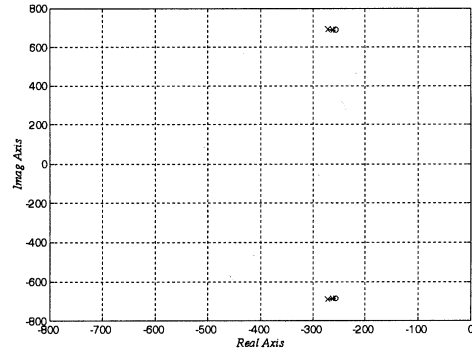
Fig. 9. Bode plot of  $\bar{\nu}_o(s)/\bar{\nu}_{in}(s)$ : (1) ZVT-PWM boost converter and (2) conventional boost converter.

$$\approx -\frac{2a_1}{L_m T_s} (R_L D') - \frac{a_2}{L_m T_s} \quad (42)$$

$$k_{2i_{Lm}} \triangleq \left. \frac{\partial \delta_{o2}}{\partial i_{Lm}} \right|_Q = \frac{L_r}{C_f T_s} \frac{I_{Lm}}{V_o} \approx \frac{L_r}{C_f T_s} \frac{1}{(R_L D')} \quad (43)$$

$$\begin{aligned} k_{2\nu_{Cf}} &\triangleq \left. \frac{\partial \delta_{o2}}{\partial \nu_{Cf}} \right|_Q = -\frac{L_r}{2C_f T_s} \left( \frac{I_{Lm}}{V_o} \right)^2 - \frac{C_s}{C_f T_s} \\ &\approx -\frac{L_r}{2C_f T_s} \frac{1}{(R_L D')^2} - \frac{C_s}{C_f T_s} \end{aligned} \quad (44)$$

with


 Fig. 10. Root locus for ZVT-PWM boost converter as a function of load  $R_L$ .

 Fig. 11. Root locus for conventional PWM boost converter as a function of load  $R_L$ .

$\delta_{o1}(t) \triangleq -v_{Cf}(t)\delta_1(t)/L_m$  and  $\delta_{o2}(t) \triangleq i_{Lm}(t)\delta_2(t)/C_f$ . Now performing Laplace transform of (40), the transfer functions from line voltage  $\tilde{v}_{in}$  and control voltage  $\tilde{v}_{ctrl}$  to output voltage  $\tilde{v}_o$

$$\frac{\tilde{v}_o(s)}{\tilde{v}_{in}(s)} = \frac{\frac{D'}{C_f L_m} + \frac{k_{2i} L_m}{L_m}}{D(s)} \quad (45)$$

and

$$\frac{\tilde{v}_o(s)}{\tilde{v}_{ctrl}(s)} = \frac{\tilde{d}(s)}{\tilde{v}_{ctrl}(s)} \frac{\tilde{v}_o(s)}{\tilde{d}(s)} = \frac{k_{PWM} I_{Lm} \left[ \left( -\frac{1}{C_f} s - \frac{r_{Lm}}{C_f L_m} + \frac{R_L D'^2}{C_f L_m} \right) + \left( \frac{R_L D'}{L_m} k_{2i} L_m + \frac{1}{C_f} k_{1i} L_m \right) \right]}{D(s)} \quad (46)$$

are obtained after some calculations, where the denominator polynomial is given by

$$D(s) \triangleq s^2 + \left[ \left( \frac{1}{R_L C_f} + \frac{r_{Lm}}{L_m} \right) - (k_{2v} c_f + k_{1i} L_m) \right] s + \left[ \left( \frac{r_{Lm}}{C_f L_m R_L} + \frac{D'^2}{C_f L_m} \right) + \left( -\frac{r_{Lm}}{L_m} k_{2v} c_f - \frac{1}{C_f R_L} k_{1i} L_m + k_{1i} L_m k_{2v} c_f + \frac{D'}{L_m} k_{2i} L_m - \frac{D'}{C_f} k_{1v} c_f - k_{1v} c_f k_{2i} L_m \right) \right] \quad (47)$$

and  $\tilde{v}_{ctrl}$  is the controller output signal applied to the input of the PWM. The small-signal gain of the PWM is given by  $k_{PWM} \triangleq \tilde{d}(s)/\tilde{v}_{ctrl}(s) = 1/V_p$  with  $V_p$  denoting the peak value of the modulating signal used in PWM [6], [7].

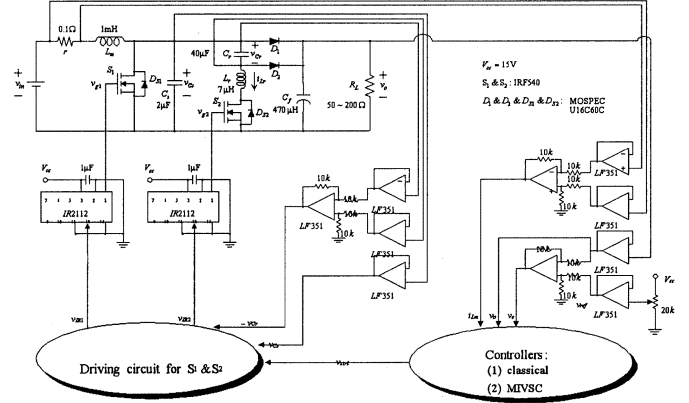
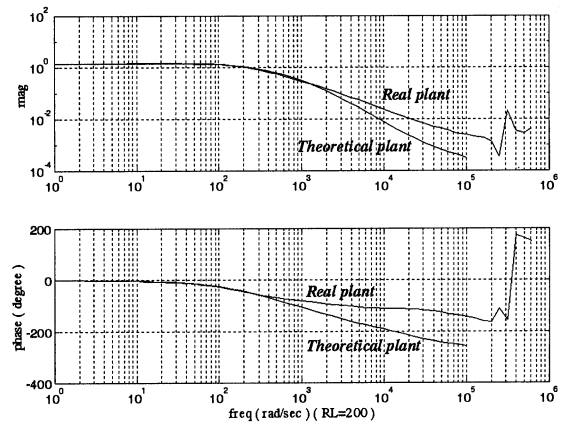


Fig. 12. ZVT-PWM boost converter with driving circuit and feedback controller.


 Fig. 13. Frequency response of  $\tilde{v}_o(s)/\tilde{v}_{ctrl}(s)$ .

## VI. COMPARISON WITH PWM BOOST CONVERTERS

It is seen from definitions (41)–(44) that all of  $k_{1i} L_m$ ,  $k_{1v} C_f$ ,  $k_{2i} L_m$  and  $k_{2v} C_f$  vanish if  $T_s$  approaches infinity. Thus the averaged mathematical model in (40) of the ZVT-PWM boost converters becomes equivalent to the averaged model of the conventional PWM boost converters.

Moreover, the pole polynomial  $D(s)$  in (47) is a function of the switching period  $T_s$ , and thus the root-locus plot of  $D(s) = 0$  with a variable parameter  $T_s$  is drawn in Fig. 7 with  $R_L = 100 \Omega$ . It reveals that the poles of the averaged model of the conventional PWM boost converter are  $s = -260.6 \pm j688.9$  with damping ratio  $\zeta = 0.354$  and natural frequency  $\omega_n = 736.6$  rad/s, as shown in Fig. 7 with  $T_s = \infty$ . For switching frequency 50 kHz, the poles of the averaged model of the ZVT-PWM boost converter are  $s = -1952$  and  $s = -266$  with damping ratio  $\zeta = 1.539$ , as shown in Fig. 7 with  $T_s = 1/50000$ .

The Bode plots of  $\tilde{v}_o(s)/\tilde{d}(s)$  and  $\tilde{v}_o(s)/\tilde{v}_{in}(s)$  of the two converters are compared, respectively, in Figs. 8 and 9 for switching frequency 50 kHz. It is seen that the ZVT-PWM boost converter exhibits better dynamical behavior with larger damping ratio.

On the other hand, variations of load resistance can also affect the poles of the boost converter. Figs. 10 and 11 show the root-locus plots for load  $R_L$  for ZVT-PWM and conventional

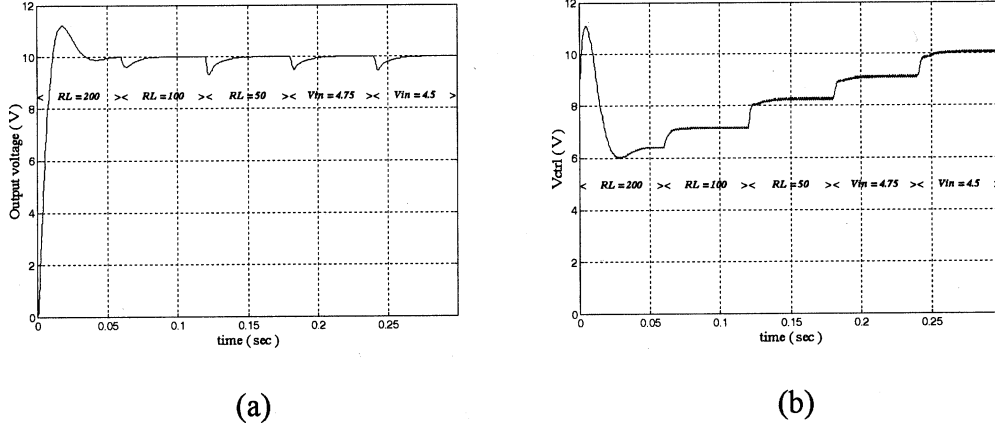


Fig. 14. Time responses of ZVT-PWM converter with classical controller  $K_{cc}(s)$ : (a) output voltage  $v_o(t)$  and (b) control signal  $v_{ctrl}(t)$ .

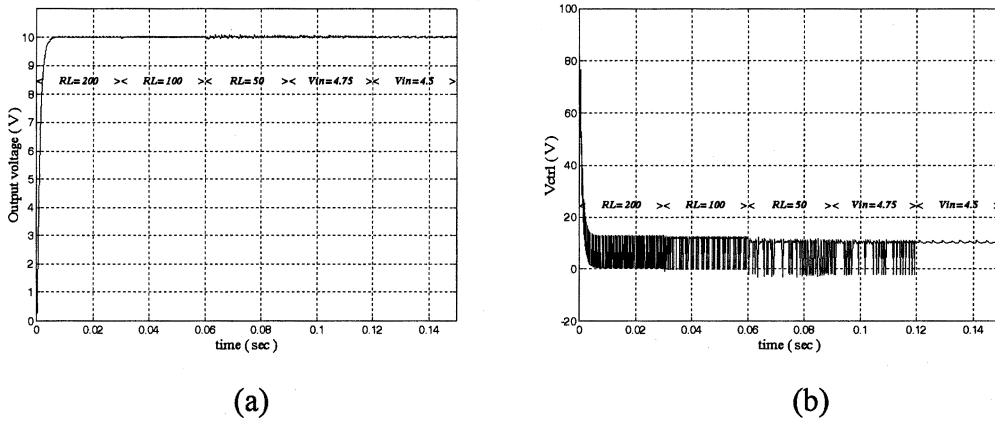


Fig. 15. Time responses of ZVT-PWM converter with MIVSC controller  $K_{mc}(s)$ : (a) output voltage  $v_o(t)$  and (b) control signal  $v_{ctrl}(t)$ .

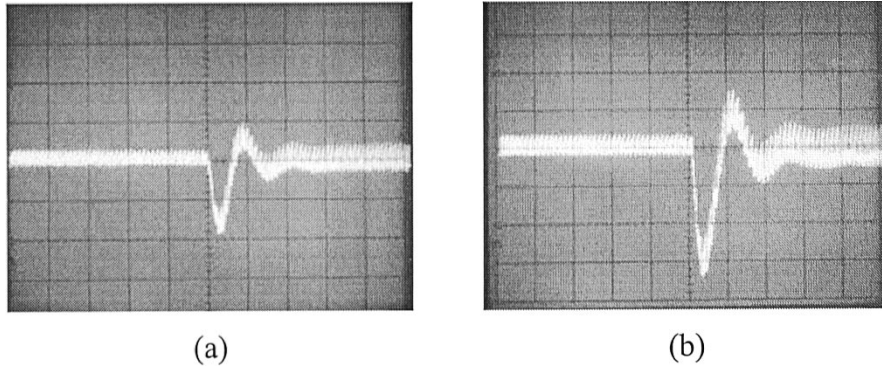


Fig. 16. Output responses of ZVT-PWM converter with classical controller  $K_{cc}(s)$  under load variations: (a)  $R_L = 200 \rightarrow 100 \Omega$ ,  $V_{in} = 5 \text{ V}$  and (b)  $R_L = 100 \rightarrow 50 \Omega$ ,  $V_{in} = 5 \text{ V}$ ; vertical: 50 mV/div, ac; horizontal: 5 ms/div.

PWM boost converters, respectively. With the variations of load  $R_L = 50 - 200 \Omega$ , the poles of the ZVT-PWM boost converter migrate from  $s = -690 \pm j292$  to  $s = -88$  and  $s = -5462$  and damping ratio  $\zeta$  changes from 0.92 to 12.46. While poles of the conventional PWM boost converter migrate from  $s = -271 \pm j692$  to  $s = -255 \pm j687$ , damping ratio  $\zeta$  changes from 0.365 to 0.348 and natural frequency  $\omega_n$  changes from 743 to 732 rad/s. It reveals that the poles of the ZVT-PWM boost converter migrate to the negative real axis in the s-plane while the poles of the conventional PWM boost converter are almost fixed. Although the poles are sensitive to the load variations,

ZVT-PWM boost converters still exhibit better dynamical characteristics due to larger damping ratio.

## VII. MODEL VERIFICATION

In this section, the derived small-signal model is verified by the experimental results. A small power prototype of the ZVT-PWM boost converter for theoretical verification is implemented with the following parameters :

- nominal input voltage  $V_{in} = 5 \text{ V}$ ;
- reference voltage  $V_{ref} = 10 \text{ V}$ ;

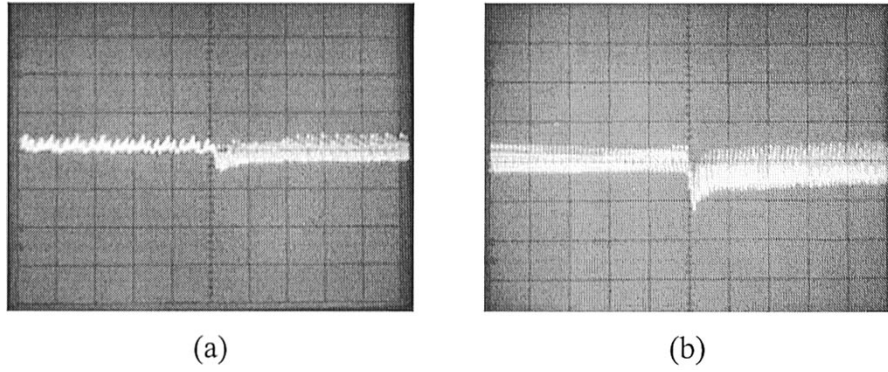


Fig. 17. Output responses of ZVT-PWM converter with MIVSC controller  $K_{mc}(s)$  under load variations: (a)  $R_L = 200 \rightarrow 100 \Omega$ ,  $V_{in} = 5 \text{ V}$  and (b)  $R_L = 100 \rightarrow 50 \Omega$ ,  $V_{in} = 5 \text{ V}$ ; vertical: 50 mV/div, ac; horizontal: 5 ms/div.

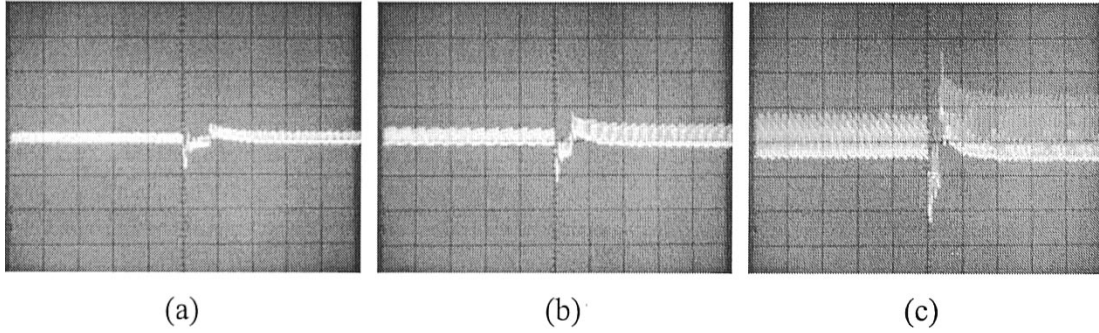


Fig. 18. Output responses of ZVT-PWM converter with classical controller  $K_{cc}(s)$  under line voltage variations  $V_{in} = 5 \rightarrow 4 \text{ V}$ : (a)  $R_L = 200 \Omega$  (b)  $R_L = 100 \Omega$ , and (c)  $R_L = 50 \Omega$ ; vertical: 50 mV/div, ac; horizontal: 50 ms/div.

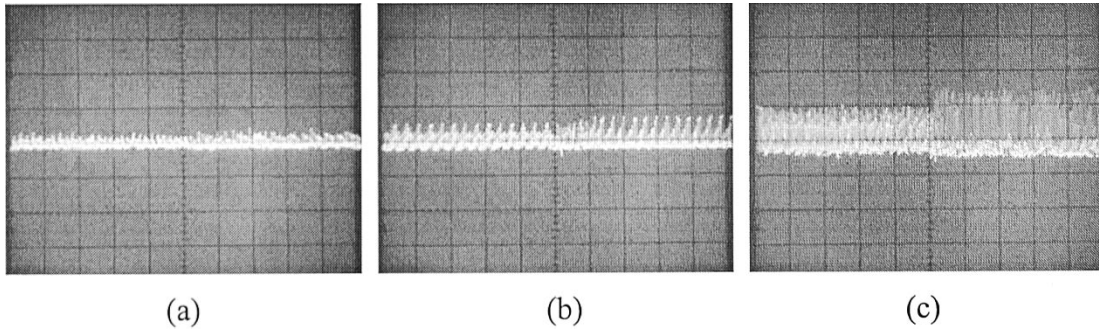


Fig. 19. Output responses of ZVT-PWM converter with MIVSC controller  $K_{mc}(s)$  under line voltage variations  $V_{in} = 5 \rightarrow 4 \text{ V}$ : (a)  $R_L = 200 \Omega$  (b)  $R_L = 100 \Omega$  and (c)  $R_L = 50 \Omega$ ; vertical: 50 mV/div, ac; horizontal: 50 ms/div.

peak of the applied ramp wave $V_p$	14 V;
load resistance $R_L$	50–200 $\Omega$ ;
input inductor $L_m$	1 mH;
output capacitor $C_f$	470 $\mu\text{F}$ ;
resonant inductor $L_r$	7 $\mu\text{H}$ ;
resonant capacitor $C_r$	40 nF;
snubber capacitor $C_s$	2 nF;
inductor series resistance $r_{Lm}$	0.5 $\Omega$ ;
switching frequency $f_s$	50 kHz;
nominal duty ratio $D$	0.5.

A driving circuit is designed so that the main switch operates under zero-voltage switching. Fig. 12 is the implemented ZVT-PWM boost converter with driving circuit and feedback controller. Substituting the above parameters and  $R_L = 200 \Omega$

into (40), the dynamical equation of the ZVT-PWM boost converter is given by

$$\dot{\tilde{x}} = \begin{bmatrix} -5539.66 & -392.33 \\ 1071.39 & -10.88 \end{bmatrix} \tilde{x} + \begin{bmatrix} 1000 \\ 0 \end{bmatrix} \tilde{v}_{in} + \begin{bmatrix} 796.05 \\ -17.21 \end{bmatrix} \tilde{v}_{ctrl} \quad (48)$$

$$\tilde{v}_o = [0 \ 1] \tilde{x} \quad (49)$$

where  $\tilde{x}(t) \triangleq [i_{Lm}(t) \tilde{v}_{cf}(t)]^T$  and  $v_{ctrl} = \tilde{d}/k_{\text{PWM}} = V_p \tilde{d} = 14\tilde{d}$ . It follows directly from (46) that the nominal transfer function is given by

$$\frac{\tilde{v}_o(s)}{\tilde{v}_{ctrl}(s)} = \frac{-17.21s + 7.575 \times 10^5}{s^2 + 5550s + 4.806 \times 10^5}. \quad (50)$$

The experimental results measured by transfer function analyzer R9211b are compared with theoretical predictions in Fig. 13. It is seen that the developed small-signal model accurately predicts the dynamical characteristics up to 1000 rad/s.

### VIII. CONTROLLERS DESIGN

In this section, two kinds of controllers will be designed for the ZVT-PWM boost converter. They are classical and MIVSC controllers.

#### A. Classical Controller Design $K_{cc}(s)$

The root-locus method is now applied to design a classical controller. A pole at  $s = 0$  is added to eliminate the steady-state error and a zero at  $s = -500$  is added to improve phase margin. Moreover, by adding a zero at  $s = -8000$  and a pole at  $s = -10\,000$ , the root loci are migrated to the left half of s-plane. As a result, a phase lead-lag controller is given by

$$K_{cc}(s) = \frac{0.5(s + 500)(s + 8000)}{s(s + 10\,000)}. \quad (51)$$

#### B. MIVSC Controller Design $K_{mc}(s)$

The MIVSC control scheme is applied to design a sliding mode controller for the ZVT-PWM boost converter in (50) with two poles at  $s_1 = -5462.5$  and  $s_2 = -87.9$ . The eigenvalues of the closed-loop system in Fig. 12 are selected at  $\lambda_1 = 0$ ,  $\lambda_2 = -1000$  and  $\lambda_3 = -7000$ . By applying eigenstructure assignment technique, the hyperplanes vector is found to be  $H = [1.61 \ 11.61 \ -10\,000]$  which yields  $u = u_{eq} + u_n$  with

$$u_{eq} = -3.26i_{Lm} - 8.53\nu_{cf} + 9.24V_{ref}, \quad u = -6\text{sgn}(\sigma). \quad (52)$$

The switching function is defined as  $\sigma \triangleq 1.61i_{Lm} + 11.62\nu_{cf} - 10\,000x_R$ , where  $x_R$  is the output state of the integrator.

To examine the performance of the closed-loop system with respect to controllers  $K_{cc}(s)$  and  $K_{mc}(s)$ , variations of load resistance and line voltage are taken into consideration. Simulation results for ZVT-PWM boost converter with classical controller  $K_{cc}(s)$  are shown in Fig. 14 with  $V_{ref} = 10\text{ V}$ . The line voltage  $V_{in}$  is initially set to 5 V and load  $R_L$  is set to 200  $\Omega$  at  $t = 0\text{ s}$ , then the load is changed to  $R_L = 100\ \Omega$  at  $t = 0.06\text{ s}$ , and at  $t = 0.12\text{ s}$ , then line voltage is changed to  $V_{in} = 4.75\text{ V}$  at  $t = 0.18\text{ s}$ , and finally  $V_{in} = 4.5\text{ V}$  at  $t = 0.24\text{ s}$ .

Simulation results for ZVT-PWM boost converter with MIVSC controller  $K_{mc}(s)$  are also shown in Fig. 15 with  $V_{ref} = 10\text{ V}$ . The line voltage  $V_{in}$  is initially set to 5 V and load  $R_L$  is set to 200  $\Omega$  at  $t = 0\text{ s}$ , then the load is changed to  $R_L = 100\ \Omega$  at  $t = 0.03\text{ s}$ , and  $R_L = 50\ \Omega$  at  $t = 0.06\text{ s}$ , then line voltage is changed to  $V_{in} = 4.75\text{ V}$  at  $t = 0.09\text{ s}$ , and finally  $V_{in} = 4.5\text{ V}$  at  $t = 0.12\text{ s}$ . It is interesting to note from the simulation results that the ZVT-PWM boost converter with MIVSC controller  $K_{mc}(s)$  exhibits excellent output voltage response which is almost independent of the variations of load resistance and line voltage.

Experimental results for load and line voltage variations are shown in Figs. 16–19 for the ZVT-PWM boost converter with

classical controller and MIVSC controller. It shows that the MIVSC controller still exhibits better performance than the classical controller.

### IX. CONCLUSION

A small-signal model of ZVT-PWM boost converters is developed in this paper. The analysis shows that ZVT-PWM boost converters exhibit better dynamical behavior than the conventional PWM boost converters. The mathematical model is verified by experimental results. With the help of this model, a classical controller and an MIVSC controller are then designed to regulate the output voltage and reject the line voltage disturbance. Results from simulations and experiments show that the MIVSC controller is better than the classical controller in the presence of variations of line voltage and load resistance.

### REFERENCES

- [1] G. Hua, E. X. Yang, Y. Jiang, and F. C. Lee, "Novel zero-voltage-transition PWM converter," *IEEE Trans. Power Electron.*, vol. 9, pp. 213–219, Mar. 1994.
- [2] B. P. Divakar and A. Ioinovici, "PWM converter with low stresses and zero capacitive turn on losses," *IEEE Trans. Aerosp. Electron. Syst.*, vol. 33, pp. 913–920, July 1997.
- [3] C. J. Tseng and C. L. Chen, "Novel ZVT-PWM converters with active snubbers," *IEEE Trans. Power Electron.*, vol. 13, pp. 861–869, Sept. 1998.
- [4] J. Sun and H. Grotstollen, "Averaged modeling of switching power converters: reformulation and theoretical basis," in *Proc. IEEE PESC*, Toledo, Spain, 1992, pp. 1162–1172.
- [5] J. L. Lin and W. J. Yang, "Modified IVSC stabilization and swing up control of an inverted pendulum," in *Proc. R.O.C. Automat. Contr. Conf.*, Taipei, Taiwan, 1997, pp. 150–153.
- [6] T. L. Chern and Y. C. Wu, "An optimal variable structure control with integral compensation for electrohydraulic position servo control systems," *IEEE Trans. Ind. Electron.*, vol. 39, pp. 460–463, Oct. 1992.
- [7] M. E. Aggoune, F. Boudjema, A. Bensenouce, A. Hellal, M. R. El-Emesai, and S. V. Vadari, "Design of variable structure voltage regulator using pole assignment technique," *IEEE Trans. Automat. Contr.*, vol. 39, pp. 2106–2111, Oct. 1994.



**Jong-Lick Lin** (M'99) was born in Tainan, Taiwan, R.O.C., in 1948. He received the B.S. and M.S. degrees in electrical engineering from National Taiwan University, Taipei, Taiwan, in 1973 and 1977, respectively, and the Ph.D. degree from the Engineering Department, Leicester University, Leicester, U.K., in 1992.

He is a Professor in the Department of Engineering Science, National Cheng Kung University, Tainan, Taiwan. His research interests include robust control theory, singular system analysis, sliding mode control, and dynamics analysis and controller design of power electronics.



**Chin-Hua Chang** was born in Taichung, Taiwan, R.O.C., in 1975. He received the B.S. degree in electrical engineering from National Sun Yat-Sen University, Kaoshiung, Taiwan, in 1997, and the M.S. degree in engineering science from the National Cheng Kung University, Tainan, Taiwan, in 1999.

His research interests include system control, sliding mode control, and power electronics system design.